UNIVERSITY OF AMSTERDAM
FACULTY OF SCIENCES

BSC THESIS BÈTA-GAMMA - PHYSICS

A RESEARCH CONDUCTED AT THE
INSTITUTE FOR MARINE AND ATMOSPHERIC RESEARCH UTRECHT

BETWEEN 1 FEBRUARY 2014 AND 18 JUNE 2014

Effect of deepening and sea level rise on tidal range in the Elbe estuary

---

Supervisors:
Prof. dr. Huib DE SWART
& MSc Erik ENSING

Author:
Roos BOL

Second supervisors:
Dr. Rudolf SPRIK
& prof. dr. Ben VAN LINDEN
VAN DEN HEUVELL

UNIVERSITEIT VAN AMSTERDAM

ABSTRACT

Increasing tidal range in the Elbe estuary constitutes a problem for shipping and the ecosystem. The increase in tidal range over the last century has been suggested to be caused by deepening activities. Besides, rising mean sea level leads to changed tidal characteristics in the North Sea, and is thus also expected to influence tidal range in the estuary. In this thesis, the effects of both deepening and sea level rise on tidal range in the Elbe estuary were investigated and compared. Tidal range was simulated using an analytical model with solutions to the width-averaged shallow water equations, and tidal forcing including the principal semi-diurnal lunar tide and its first overtide. This was done for three different depth configurations. The model was found to reasonably represent current tidal range in the estuary. The results suggest that deepening of the estuary up to Hamburg will result in a further increase of tidal range, especially in the region around Hamburg. Global sea level rise, as estimated by the IPCC for 2100, was found to lead to an increase in M2 and M4 amplitudes at Cuxhaven, resulting in an along-estuary increase in tidal range. The maximum increase of tidal range due to deepening and expected sea level rise was comparable in size. The research shows that the combined long-term effects of both deepening and sea level rise should be studied before new dredging activities are carried out in the Elbe estuary. Lastly, possible improvements to the model are discussed.

Populair-wetenschappelijke samenvatting

De Elbe is een estuarium in Duitsland, dat uitmondt in de Noordzee. De waterdynamica wordt hier in grote mate bepaald door het getij: het effect van eb en vloed is merkbaar tot zo'n 140 km landinwaarts, waar een dam de getijgolven tegenhoudt. De afgelopen eeuw is er een sterke toename geweest in het getijdenverschil in de Elbe; waterstanden bij vloed werden steeds hoger, en bij eb juist steeds lager. Dit heeft nadelige gevolgen voor de scheepvaart en voor het ecosysteem. Bij lage waterstanden kunnen grote schepen niet passeren en gaat de zuurstofconcentratie in het water omlaag, wat schadelijk kan zijn voor planten en dieren.

FIGUUR: De Elbe van bovenaf gezien. Het getij komt bij Cuxhaven het estuarium binnen vanuit de Noordzee, en zorgt voor een duidelijk merkbaar getijdenverschil tot 140 km landinwaarts, waar de dam in Geesthacht de getijgolf tegenhoudt.

Een mogelijke oorzaak voor de toename in getijdenverschil is de steeds verdere verdieping van het kanaal, die in de afgelopen eeuw uitgevoerd werd om de haven van Hamburg bereikbaar te houden voor vrachtschepen. Hoe komt dat nu precies?

Het getij kan beschreven worden als een golf, met een golflengte van enkele honderden kilometers en een periode van iets meer dan 12 uur. Een getijgolf die het estuarium binnenkomt, wordt gereflecteerd tegen de dam. De inkomende en gereflecteerde golf interfereren met elkaar, waardoor een staande golf kan ontstaan. Dit verschijnsel wordt ook wel resonantie genoemd. Of resonantie optreedt is afhankelijk van de breedte, de lengte en de diepte van het estuarium. De situatie is vergelijkbaar met resonantie van een geluidsgolf in een orgelpijp, met één gesloten uiteinde. Hoe dichter een estuarium bij resonantie is, hoe hoger het getijdenverschil zal zijn. Daarnaast is het Elbe estuarium bovendien convergent: de breedte neemt af naarmate je verder landinwaarts gaat.

Ook dit zorgt voor een verhoging van het getijdenverschil landinwaarts, omdat dezelfde hoeveelheid water door een steeds smaller kanaal gestuwd wordt.

Behalve door resonantie en convergentie, zal het getij in de toekomst waarschijnlijk beïnvloed worden door zeespiegelstijging. Als de zeespiegel in de Noordzee stijgt, heeft dit gevolgen voor de karakteristieken van de getijgolf die vanuit de Noordzee de Elbe ingaat, en hier het getijdenverschil veroorzaakt. Volgens de IPCC zal de zeespiegel over de hele wereld in 2100 waarschijnlijk een halve meter gestegen zijn, en in het ergste geval zelfs één meter.

In dit onderzoek worden de effecten van zowel verdieping als zeespiegelstijging op het getijdenverschil in de Elbe onderzocht en vergeleken. Hiervoor wordt een stelsel van vergelijkingen, de ondiep water vergelijkingen genaamd, opgelost en gesimuleerd in een analytisch model.

Uit de resultaten van de simulatie blijkt dat zowel zeespiegelstijging als verdieping in de Elbe zullen leiden tot een verdere toename van het getijdenverschil. Het onderzoek maakt duidelijk dat het belangrijk is om de lange termijn effecten van zowel verdieping als zeespiegelstijging goed te onderzoeken, voordat verdere plannen voor verdieping van de Elbe ten uitvoer gebracht worden.

Aantal woorden: 579

ACKNOWLEDGEMENTS

Contents

1 | Introduction

The Elbe estuary is situated in Germany and connected to the North Sea, where tides play a prominent role in the water dynamics. The estuary is of great ecological value, with over 30 nature protection areas along its shores and vast shallow water areas that are important for fish and bird populations (Deltares, 2011). With the transport hub of Hamburg 100 km inland from the sea, the Elbe estuary also serves as an important transport channel for large vessels on their way to the port of Hamburg.

In the past century, the shape of the estuary has been heavily modified by human interventions. In 1960, a weir was built at Geesthacht, 140 km up-estuary, and in the 1980s large dyke constructions were built along the shores. Since the beginning of the twentieth century, the estuary has been deepened several times to ensure a navigable channel for ships of growing size (Kerner, 2014; Kappenberg and Fanger, 2007; Winterwerp et al., 2013). At the same time, an increase in tidal range has been observed over the last decades (Winterwerp et al., 2013; HPA and MOW, 2013). The increased tidal range constitutes danger of flooding and is a potential problem for shipping. If water levels are too low, ships cannot proceed to and from the habrour of Hamburg. Furthermore, the strong variations in water level can pose a threat to fragile ecosystems along the estuary (Deltares, 2011).

Winterwerp et al. (2013) suggested that the increase in tidal range is caused by tidal resonance due to reflections of tidal waves at the weir. This reflection causes standing wave-behavior, which can have a significant effect on tidal range and velocity (Winterwerp and Wang, 2013). Resonance characteristics depend largely upon estuary geometry, and are therefore influenced by human modifications to estuary depth, width or length (De Jonge et al., 2014)

This research focuses on the underlying physical mechanisms of resonance characteristics in the Elbe estuary. As described above, estuary geometry plays an important role. A second mechanism affecting tidal characteristics is sea level rise. Mudersbach et al. (2013) use long-term tidal gauge data and sea-level records to show that there is a significant correlation between sea level rise and increasing tidal range at the moth of the Elbe estuary. Pickering et al. (2012) reach the same conclusion for the impact of future sea-level rise, based om model simulations of the European shelf tides.

In this research, the effect of both deepening and sea level rise on tidal range in the Elbe estuary is investigated. To assess the impact of both deepening and sea level rise, tidal response of the estuary is simulated using an analytical model containing solutions of the

linearised shallow water equations. The model is applied to three different configurations of the longitudinal bottom profile. Firstly, the modelled tidal range for each configuration will be compared to measurements, to determine which aspects are well reproduced by the model. Next, the effect of deepening on tidal range will be investigated for all three configurations. Lastly, the effect of sea level rise on tidal range will be investigated for the same three configurations, using estimates for sea level rise in 2100 from the last IPCC assessment report in Church et al. (2013). Since sea level rise will most likely have a significant impact on the tidal forcing of the Elbe estuary, modelled changes in external tidal forcing will also be included. The effects of deepening and sea level rise will then be compared to each other.

In the next section, a theoretical framework for this research will be described, including the model equations that were used. This is followed by a description of the research method in section 3. In section 4, simulation results for the three bottom configurations will be compared to measured values, and the results of both the influence of deepening and sea level rise will be quantified and compared to each other. The thesis ends with a discussion of these results and concluding remarks.

2 | Theory

This section provides a theoretical framework for the conducted research. Firstly, the theory behind the generation of tides and different tidal constituents is explained. Next, the shallow water equations will be introduced to describe what happens when the generated tidal wave enters the estuary at the open boundary. The dominant factors determining tidal response of the estuary will be discussed, and eventually, a solution to the linearised shallow water equations will be given.

2.1 Generation of tides

2.1.1 Equilibrium tides

The principal generation of the tide arises from the dynamics of the moon-earth system, rotating about a common centre of mass (Open-University, 2001). This causes a centrifugal force that is equal in each point on the earth's surface and points away from the moon. The vector sum of the centrifugal and gravitational force acting on the earth in this system is the tide-producing force, that is different depending on the location on the earth's surface. Since the moon rotates about the common centre of mass every 27.3 days in the same direction as the earth rotates about its own axis, the period of the earth's rotation with respect to the moon is 24 hours and 50 minutes. This period is called the lunar day.

In figure 2.1, the generation of the lunar tide is illustrated. The tidal bulge closest to the moon is caused mainly by gravitational attraction; the tidal bulge furthest from the moon by centrifugal acceleration. During a complete earth rotation, one point on the surface of the earth experiences two high tides, indicated with 1 and 3, and two low tides, indicated with 2 and 4. This is called the semi-diurnal lunar tide and is also referred to as the M2-tide (Open-University, 2001).
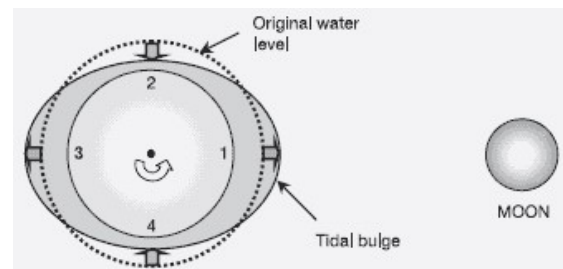
FIGURE 2.1: Generation of tidal bulges in the moon-earth system (tidal bulges are exaggerated). A point on the surface of the earth experiences two high tides (1 & 3) and two low tides (2 & 4) during each complete earth rotation with respect to the moon.
Source: Garrison (2007)

A similar force balance exists for the sun-earth system, causing the principal solar or S2-tide. In the North Sea, however, S2 amplitudes are small compared to M2 amplitudes. This research therefore focuses on the lunar tide only. The theory of the interacting

system of lunar and solar tides is also called the equilibrium tide theory (Open-University, 2001). However, equilibrium tides do not occur on earth for several reasons, as will be explained in the next section.

2.1.2 Dynamic tides and overtides

Due to the constraints of land masses and the non-uniform depth of oceans, tides on earth will deviate from equilibrium tides. When associated non-linear processes are included, the ocean dynamics are described by the dynamic theory of tides. The speed of a travelling tidal wave is controlled by water depth; a wave travelling over continental shelf regions and in shallower coastal waters will be slowed down. Since the top part of the wave effectively experiences a greater water depth, it will travel faster than the lower part of the wave. Thus, inertia will cause the tidal wave to deviate from the harmonic tidal wave, as is described in detail in the review by Friedrichs (2004). A Fourier time series of the principal tide will arise, with terms representing overtides with frequencies that are multiples of the principal frequency. The lunar overtides are known as the M4-tide, M6-tide, etcetera. The M4-tide, for example, is the first harmonic overtide of the M2-tide, and thus has a frequency that is twice the M2 frequency. Overtides originate from non-linear dynamics in shallow water. The process of advection, for example, is the source of even overtides such as M4.

This research focuses on the Northwest European shelf, where the tide is dominated by the M2-tide. Therefore, only the M2-tide and it's first harmonic overtide, the M4-tide, were included in this research.

2.1.3 Amphidromic systems

As stated before, the restriction of tidal waves by land masses on earth results in complex ocean dynamics. A second factor determining ocean dynamics is the Coriolis force. The Coriolis force arises from the application of Newton's laws of motion to a rotating frame of reference. As is shown in e.g. Marshall and Plumb (2008), the Coriolis acceleration $\vec{a}_c$ is given by

$$\vec{a}_c = -2\vec{\Omega} \times \vec{u}, \tag{2.1}$$

where $\vec{u}$ is the velocity of the moving object in the rotating frame, and $\vec{\Omega}$ is the angular velocity vector. The Coriolis force is in fact a fictitious force; it does no work, but merely acts to change the direction of flow.

Since the earth rotates around its axis only once per day, the Coriolis acceleration due to earth rotation is relatively small, and is only noticeable for motions occurring over large distances and timescales longer than a day (Marshall and Plumb, 2008). The Coriolis effect plays a significant role in the deflection of tidal waves. For anti-clockwise rotation,
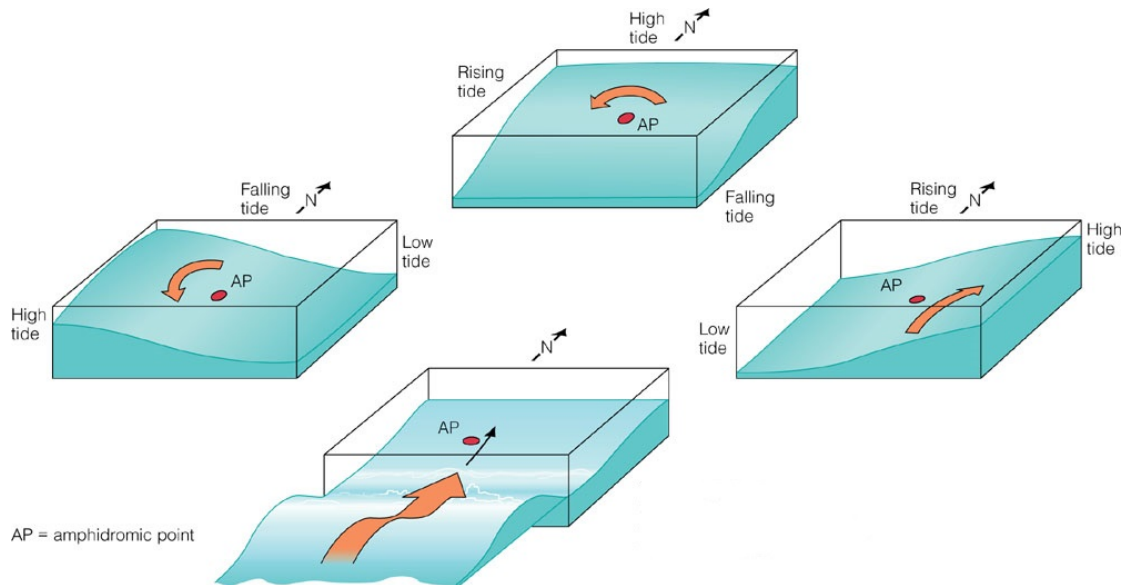
FIGURE 2.2: Manifestation of an amphidromic point. The tidal crest enters a basin and, on the northern hemisphere, is deflected anti-clockwise due to the Coriolis effect. A resulting node or amphidromic point in the middle of the basin develops.
Source: Garrison (2007)

like the earth's rotation, $\vec{\Omega}$ is positive. A fluid parcel of the tidal wave moving in a plane perpendicular to the earth's surface is thus deflected to the right on the northern hemisphere. On the southern hemisphere, the fluid parcel is deflected to the left.

Together with the constraint of land masses, the Coriolis effect results in the development of amphidromic points in oceans and coastal waters (Open-University, 2001). This process is illustrated in figure 2.2. If a tidal wave enters a basin, the Coriolis effect deflects the wave to the right on the northern hemisphere. The reflected wave also tends to the right, and thus, the water spins around the basin; anti-clockwise on the northern hemisphere, and clockwise on the southern hemisphere. The resulting node in the middle of the basin experiences no tidal range, and is called an amphidromic point (Garrison, 2007). Tidal range thus increases with distance from an amphidromic point.

Tidal waves in amphidromic systems are classified as Kelvin waves, for which the amplitude is greatest near coasts Open-University (2001). This can

FIGURE 2.3: Amphidromic points in the North Sea. Co-tidal lines are shown in red, with numbers indicating the time of high water (in hours) after the moon has passed the Greenwich meridian. Blue lines represent co-range lines, with tidal range in meters.
Source: Open-University (2001)

also be seen from figure 2.2. Kelvin waves occur at the equator and at coasts, where the deflection by the Coriolis force is zero or constrained, respectively. In figure 2.3, the amphidromic system of the North Sea is shown as an example. Marshall and Plumb (2008) describe that amphidromic points only appear in basins with a width much smaller than the Rossby deformation radius, $\sqrt{gh}/\Omega$. This means that in the North Sea, amphidromic points can be observed, whereas in the Elbe, they only manifest themselves as nodal lines.

2.2 Tides in estuaries

2.2.1 Shallow water equations

In estuaries, water depth, or the vertical length scale, is typically much smaller than horizontal length scales, such as basin length or tidal wavelengths. This justifies the use of the shallow water equations as described by e.g. Marshall and Plumb (2008). The shallow water equations are a set of partial differential equations derived from depth-integrating the Navier-Stokes equations. They express the time rate of change of both the free surface elevation η and the width-averaged tidal velocity u in two different equations: the mass balance and the momentum balance (Marshall and Plumb, 2008).

Since this research focuses on the underlying physical processes of the water motion, the shallow water equations were linearised to make them analytically solvable. Linearisation is possible here because tidal amplitudes are small compared to water depth, allowing for the application of perturbation theory (Friedrichs, 2004). In the following section, the equations for η and u are already linearised; the details of this linearisation process are explained in appendix A.

In this research, the variation of η and u in the along-channel x-direction is investigated. The vertical velocity profile, or velocity variation in z-direction, is also taken into account. The linearised mass balance or continuity equation then reads

$$\frac{\partial(b\eta)}{\partial t} + \frac{\partial}{\partial x}\left(b \int_{-h}^{0} u \ \mathrm{d}z \right) = 0, \qquad (2.2)$$

where b is the width of the estuary. This equation has the form of a general conservation equation; the total change in the cross-sectional area must equal the divergence of the total volume transport (Marshall and Plumb, 2008). The conservation of mass that formula 2.2 expresses, is illustrated in figure 2.4.
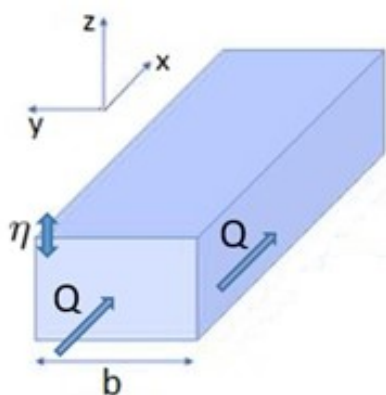
FIGURE 2.4: Mass conservation as stated in equation 2.2. Changes in surface elevation η result in a change in the perpendicular surface; this results in a change in the total volume transport $Q = b \int_{-h}^{0} u \ \mathrm{d}z$.

The second equation is the momentum balance, which expresses the time rate of change of the tidal velocity in terms of the relevant physical processes. As described by Friedrichs (2004), the linearised, cross-sectionally averaged momentum equation reads

$$\frac{\partial u}{\partial t} = -g\frac{\partial \eta}{\partial x} + \frac{\partial}{\partial z}\left(A_v\frac{\partial u}{\partial z}\right), \tag{2.3}$$

where g is the gravitational acceleration and A_v the vertical eddy viscosity. The terms on the right-hand side of equation 2.3 represent, from left to right, along-channel pressure gradient and internal friction. Internal friction is usually expressed using the shear stress or force per unit area τ_{xz}, which is a measure for the transport of x-momentum in the z-direction, when different 'slabs' of water slide over one another (Marshall and Plumb, 2008). The force per unit area per unit mass depends on the velocity profile in z-direction. For higher vertical variations of u, the shear stress, divided by the density ρ, will be bigger. Therefore, $\frac{\tau_{xz}}{\rho}$ is parametrised in equation 2.3 as $A_v\frac{\partial u}{\partial z}$, with the eddy viscosity A_v as proportionality constant, which for now will be assumed constant over the whole estuary.

From the mass and momentum balance, all relevant physical effects can be derived. To solve the equations, boundary conditions need to be specified, which will be done in section 2.2.4. But firstly, two processes that are dominant in determining the estuary tidal response will be examined: resonance and width convergence.

2.2.2 Resonance

An important factor determining tidal elevation and velocity in an estuary is resonance. A tidal wave entering the estuary at the open boundary can be reflected against a barrier up-estuary, such as a weir, and cause standing wave behavior (Open-University, 2001). For certain wavelengths, resonance can occur, resulting in maximum amplification and
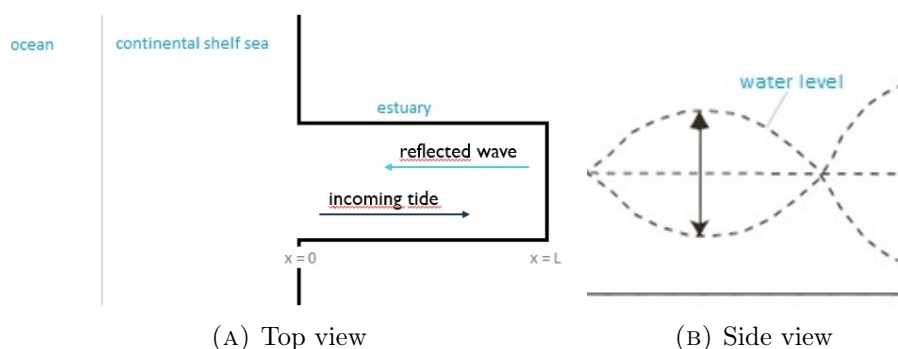

(A) Top view   (B) Side view

FIGURE 2.5: View from top and side of an estuary or bay showing the occurrence of resonance. When a tidal wave propagates through the estuary, resonance can occur due to reflection at a closed boundary and a standing wave can form. Figure (B) shows resonance for an estuary length that is $\frac{3}{4}$ of the tidal wavelength.

damping of the tidal wave as illustrated in figure 2.5. The physical situation is comparable to the propagation of a sound wave through an organ pipe with one open end. In appendix B, the resonance condition for a straight, frictionless estuary is derived from the shallow water equations given in equation 2.2 and 2.3, resulting in

$$\frac{\omega L_c}{\sqrt{gh}} = (n - \frac{1}{2}\pi), \text{ for } n = 1, 2, ..., \tag{2.4}$$

where ω is the angular frequency of the tidal wave, L_c is the estuary length, g the gravitational acceleration and h the depth of the estuary. This result shows that resonance characteristics are also influenced by depth. Using that the wave period T is equal to $\frac{2\pi}{\omega}$, and that the wave speed of a shallow water wave is $\sqrt{gh}$ as given by Open-University (2001), equation 2.4 can be rewritten as

$$L_c = \left(\frac{n}{2} - \frac{1}{4}\right)\sqrt{gh}\ T = \left(\frac{n}{2} - \frac{1}{4}\right)L_t, \tag{2.5}$$

where L_t is the tidal wavelength. In figure 2.6, the ratio of water level η at the end and at the beginning of the estuary is plotted against $\frac{L_c}{4L_t}$. Resonance occurs for $\frac{L_c}{4L_t} = 2n - 1 = 1, 3, 5, ...$. In the case of no friction, as shown in the figure, the amplification of the water level is infinitely high. If friction is present, the peaks become finite, and for successive peaks, representing higher harmonics, η will be damped more strongly.
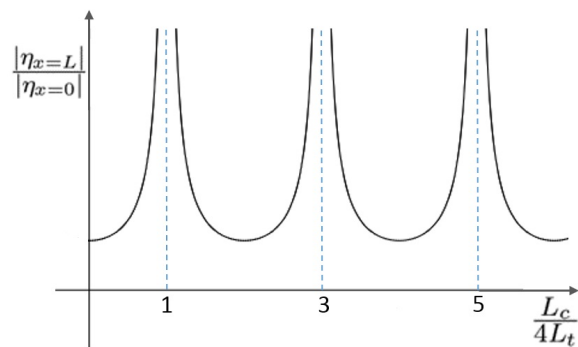
FIGURE 2.6: Ratio of water level η at the end and at beginning of the estuary $\left(\frac{|\eta_{x=L}|}{|\eta_{x=0}|}\right)$ plotted against $\frac{L_c}{4L_t}$, for a frictionless, straight estuary. The occurrence of resonance for $L_c = \left(\frac{n}{2} - \frac{1}{4}\right)L_t$ can be seen.

2.2.3 Width convergence

A second important factor influencing tidal elevation and velocity in an estuary is width convergence. Most estuaries are funnel-shaped, meaning their width converges when travelling up-estuary, as shown in figure 2.7. For an exponentially converging estuary, the width b is given by

$$b = b_0 \cdot e^{\frac{-x}{L_b}}, \tag{2.6}$$

where b_0 the width of the estuary at the open boundary and L_b is the e-folding convergence length. This is the length over which the estuary width decreases by a factor e. In case of no reflection, the effect of convergence is to increase tidal range up-estuary, since the same volume of water must travel through a smaller passageway.

As described by Friedrichs (2004), convergence in combination with resonance causes dynamics that are less easily predicted. The incoming wave is amplified due to the narrowing channel. The reflected wave experiences a widening channel as it propagates back through the estuary, and is thus dampened. The incoming and reflected wave interfere, and there exists an optimal value of L_b for which tidal amplification is maximal. Convergence combined with resonance can thus

FIGURE 2.7: Schematic representation of a converging estuary with estuary length L_c and width b_0 at $x = 0$. Also shown is the e-folding convergence length L_b, which is the length over which the estuary width decreases by a factor e.

result in both dampening and amplification. In addition, both the incoming and reflected wave will be dampened if friction effects are also included.
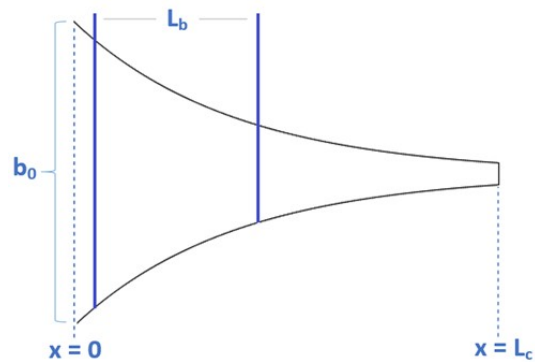
2.2.4 Solutions of the shallow water equations in a tidal estuary

In the former two sections, a closer look was taken at two of the relevant physical processes in the tidal response of the estuary. Combining these two effects in equation 2.2 and 2.3, the total response can be determined, using four different boundary conditions.

At the open boundary, where $x = 0$, the water motion is driven by a forced tidal wave of the form

$$\eta = \eta_{M2} \cos(\omega t) + \eta_{M4} \cos(2\omega t - \phi), \qquad \text{at } x = 0. \tag{2.7}$$

In appendix C, more details about the phase difference ϕ are given. It should be noted that the forcing consists of different tidal constituents, as described in section 2.1.2. In this research, only the M2 and M4 components were included. By the method of separation of variables it can be shown that the set of equations can be solved independently for each tidal constituent. Therefore, only the derivation for the M2 tide will be shown here; the derivation for M4 is analogous to this. For M2 separately, the boundary condition is

$$\eta = \eta_{M2} \cos(\omega t), \qquad \text{at } x = 0. \tag{2.8}$$

The second and third boundary conditions state that

$$u = 0, \qquad \begin{cases} \text{at } x = L_c, \\ \text{at } z = -h. \end{cases} \tag{2.9}$$

The first of these conditions sets the velocity at the closed boundary to zero, and the second is a no-slip condition, meaning the velocity is also zero at the estuary bottom.

The last boundary condition states that the shear stress τ_{xz} at the free surface vanishes:

$$A_v \frac{\partial u}{\partial z} = 0, \qquad \text{at } z = 0. \tag{2.10}$$

where the free surface is taken at $z = 0$ because of linearisation; for details, see appendix A. The non-transient solution, after the system has had time to reach equilibrium, should represent a wave of the form

$$\begin{aligned} \eta &= \eta_{c,M2}(x)\cos(\omega_{M2}t) + \eta_{s,M2}(x)\sin(\omega_{M2}t) \\ &= \mathrm{Re}\{\hat{\eta}_{M2}(x)e^{-i\omega_{M2}t}\} \end{aligned} \tag{2.11}$$

$$\begin{aligned} u &= u_{c,M2}(x,z)\cos(\omega_{M2}t) + u_{s,M2}(x,z)\sin(\omega_{M2}t), \\ &= \mathrm{Re}\{\hat{u}_{M2}(x,z)e^{-i\omega_{M2}t}\}, \end{aligned} \tag{2.12}$$

where $\hat{\eta}$ and $\hat{u}$ are complex and no longer depend on time. The total solution is a linear combination of both the M2 and M4 solutions. Implementing the solutions for M2 into equation 2.2 and 2.3, the resulting time-independent equations are

$$-i\omega b\hat{\eta} + \frac{\partial}{\partial x}\left(b \int_{-h}^{0} \hat{u}\ \mathrm{d}z\right) = 0, \tag{2.13}$$

$$i\omega\hat{u} + A_v \frac{\partial^2 \hat{u}}{\partial z^2} = g\frac{d\hat{\eta}}{dx}. \tag{2.14}$$

Right now, a set of equations that can be solved analytically is finally obtained. The second equation is a nonhmonegenous, linear differential equation, of which the general solution is the sum of the homogenous and the particular solution (Kreyszig, 2006). Introducing the constant γ as

$$\gamma = \sqrt{\frac{-2i\omega}{A_v}}, \tag{2.15}$$

the particular and homogenous solution for $\hat{u}$ are given by

$$\hat{u}_{part} = \frac{g}{i\omega}\frac{d\hat{\eta}}{dx}, \tag{2.16}$$

$$\hat{u}_{hom} = Ae^{\gamma z} + Be^{-\gamma z}, \tag{2.17}$$

where A and B are proportionality constants determined by the boundary conditions. Taking a general solution of the form $\hat{u}_{part} + \hat{u}_{hom}$ and implementing the boundary conditions from equation 2.9, the final solution reads

$$\hat{u} = \frac{g}{i\omega}\frac{d\hat{\eta}}{dx}\ p(z), \qquad \text{with } p(z) = 1 - \frac{\cosh(\gamma z)}{\cosh(\gamma h)}. \tag{2.18}$$

Substitution of this solution in equation 2.13 yields an analytically solvable equation for η that reads

$$-i\omega b\hat{\eta} + \frac{\partial}{\partial x}\left(b\frac{g}{i\omega}\frac{d\hat{\eta}}{dx}\int_{-h}^{0}p(z)\,dz\right) = 0. \tag{2.19}$$

The integral in this equation can be written as

$$P_h = \int_{-h}^{0}p(z)\,dz = \frac{h - \tanh(\gamma h)}{\gamma}. \tag{2.20}$$

Substituting this P_h and $b = b_0 e^{\frac{-x}{L_b}}$ in equation 2.19, working out the derivative and dividing by $-i\omega b$ gives the final equation

$$\kappa^2\hat{\eta} + \frac{d^2\hat{\eta}}{dx^2} - \mu\frac{d\hat{\eta}}{dx} = 0, \tag{2.21}$$

where the constants κ and μ are introduced as

$$\kappa^2 = \frac{\omega^2}{gP_h}, \qquad \mu = \frac{1}{L_b}. \tag{2.22}$$

Note that μ is real and that κ is a complex wave number; the equation for κ gives a dispersion relation for the tidal wave. The boundary conditions for $\hat{\eta}$ are

$$\hat{\eta}\bigg|_{x\,=\,0} = \hat{\eta}_{M2}, \qquad \frac{d\hat{\eta}}{dx}\bigg|_{x\,=\,L_c} = 0. \tag{2.23}$$

The first of these conditions is derived from equation 2.8 and gives the amplitude of $\hat{\eta}$ at the open boundary (shown here for the M2 tide). The second condition states that $\hat{\eta}$, just like η, must have a maximum at the closed boundary of the estuary, where $x = L_c$. Implementing these boundary conditions and solving equation 2.21 for $\hat{\eta}$ results in

$$\hat{\eta}(x) = \frac{\hat{\eta}_{M2}\,e^{\frac{-\mu x}{2}}\,[2\alpha\cos(\alpha(L_c - x)) + \mu\sin(\alpha(L_c - x))]}{2\alpha\cos(\alpha L_c) + \mu\sin(\alpha L_c)}, \tag{2.24}$$

where the constant α is introduced as

$$\alpha = \sqrt{\kappa^2 - \frac{1}{4}\mu^2}, \tag{2.25}$$

representing the complex wave number in case of convergence. Although this result looks cumbersome, it can be checked that this formula for $\hat{\eta}$ exhibits the desired physical behaviour. This is most easily done for a non-converging estuary, in the limit $\mu \to 0$. In this limit, $\alpha = \kappa$ and equation 2.24 simplifies to

$$\hat{\eta}(x) = \hat{\eta}_{M2}\left(e^{i\kappa x} + e^{-i\kappa x}\right) \tag{2.26}$$

Referring back to equation 2.11, the expression for the non-complex amplitude η is

$$\eta = \text{Re}\{\hat{\eta}(x)e^{-i\omega t}\} \tag{2.27}$$

$$= \text{Re}\{\hat{\eta}_{M2}\ (e^{i(\kappa x - \omega t)} + e^{-i(\kappa x - \omega t)})\} \tag{2.28}$$

$$= \eta_{M2}(\cos(\kappa x - \omega t) + \cos(\kappa x + \omega t)), \tag{2.29}$$

where the first cosine represents a wave travelling in positive x-direction, and the second cosine represents the reflected wave, travelling in the negative x-direction.

The solution for u can now be obtained by substituting the expression found for $\hat{\eta}$ in equation 2.18.

2.2.5 Formulation of eddy viscosity

In the derivation given above, eddy viscosity was assumed constant over the whole estuary. In practice, however, vertical eddy viscosity has been observed to scale with the velocity u and the depth h_{max}. As described by e.g. Friedrichs (2004), the linearised eddy viscosity can therefore be parametrised as $A_v = c_v \cdot |u| \cdot h_{max}$, where the bottom drag coefficient c_v is a constant of the order 10^{-2} to 10^{-3}, depending on bottom roughness scale. Taking for $|u|$ a velocity that is representative for the estuary, A_v can now be obtained globally in simulations. In this research, the representative velocity $|u|$ was taken at $(x, z) = (0, 0)$; this is the surface velocity at the seaward boundary of the estuary. Since this value of $|u|_0$ is higher than the average velocity over the estuary, this might lead to a slight overestimate of the effect of friction. Therefore, the drag coefficient c_v was modified to better match experimental data.

2.3 Tidal range

As explained in appendix C, the total water elevation is given by

$$\eta_{total}(x, t) = \eta_{M2}(x)\cos(\omega_{M2}t) +$$
$$\eta_{M4}(x)\cos(2\omega_{M2}t - \phi) \tag{2.30}$$

Due to the phase difference ϕ, this function is asymmetric, as can be seen in figure 2.8. This figure shows the surface elevation η_{total} for $x = 0$ in the Elbe estuary. The tidal range is defined as the difference between the
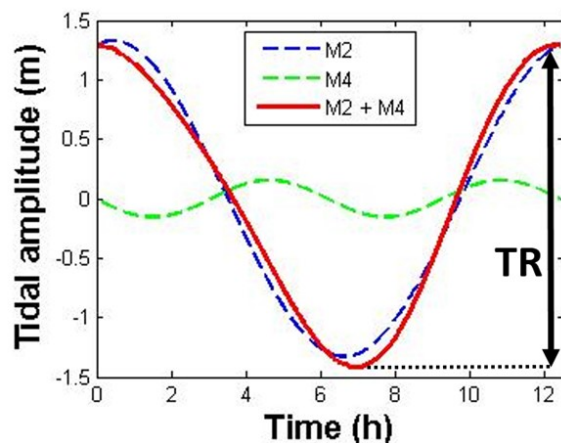

FIGURE 2.8: Total surface elevation (red line) due to M2 and M4 as a function of time, at the seaward boundary of the Elbe estuary ($x = 0$). The black arrow indicates tidal range (TR).

maximum and minimum amplitudes of η_{total}. As the M2 and M4 wave travel up-estuary, the amplitude and phase of both tidal waves will be altered as described by the shallow water equations, resulting in different tidal range for each x-location.

2.4 Sea level rise

For the last centuries, global mean sea level (MSL) has been rising steadily, as shown in figure 2.9, obtained from the fifth IPCC assessment report by Church et al. (2013). Due to carbon dioxide emissions and resulting global warming, the IPCC predicts an increase in yearly sea level rise for the upcoming decades, differentiating between five different emission scenarios. In the scenario with lowest emissions, the predicted rise in MSL is 28-61 cm by 2100, with a best estimate of 44 cm. In this scenario, emissions

FIGURE 2.9: Past and future sea level rise as predicted by Church et al. (2013). For the past, proxy data are shown in light purple and tidal gauge data in blue. Future predictions are shown in red for a very high emissions scenario, and in blue for a very low emissions scenario. Source: Church et al. (2013) fig. 13.27

are strongly reduced in the next decades, resulting in zero emissions worldwide by 2070, and successive active carbon dioxide removal from the atmosphere. For the scenario with very high emissions, indicated by the red line in figure 2.9, a rise in MSL of 52-98 cm is predicted, with a best estimate of 74 cm.

According to Church et al. (2013), strong local differences in sea level will occur for a global sea level rise. This is due to changes in the amphidromic systems of seas and oceans, since the ocean basin geometry will change if sea level rises. Mudersbach et al. (2013) show that in the North Sea, there is a significant correlation between mean sea level rise and increasing amplitudes of the M2 tidal constituent, based on Cuxhaven tidal gauge data of the last 50 years. These results are supported by Pickering et al. (2012), who performed simulations of tides in the North Sea with a numerical model and concluded that for a rising MSL, the position of the M2 amphidrome in the southern North Sea changes. According to their research, this would result in large increases in the M2 amplitude along the coast; at Cuxhaven, they predicted a rise in M2 amplitude of 0.35m for a rise in MSL of 2m. These results indicate that a rise in global MSL is likely to induce changes in the tidal forcing at the open boundary of the Elbe estuary.
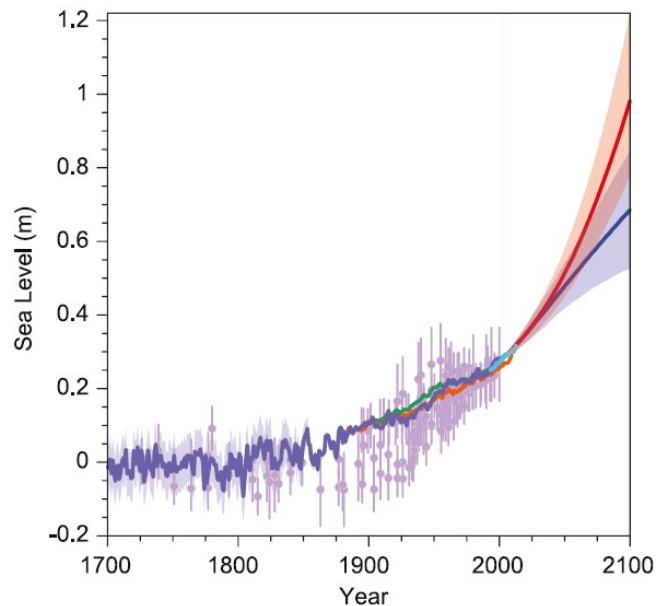
3 | Method

This section will explain the method that was used to conduct this research. Tidal response of the Elbe estuary was simulated using an analytical model, with 1D tidal elevations and one longitudinal tidal velocity component, varying in vertical direction). The characteristics and equations of the model were described in the theory section. This model was used firstly to assess the effect of deepening on tidal characteristics in the estuary. Three different scenarios for deepening were investigated. Secondly, the effect of sea level rise on tidal characteristics was simulated, using two different scenarios for sea level rise.

In this section, the modelled geometric characteristics of the Elbe estuary will be described, followed by a description of the model and relevant model equations. Then, a more detailed explanation of the experimental setup will be given.
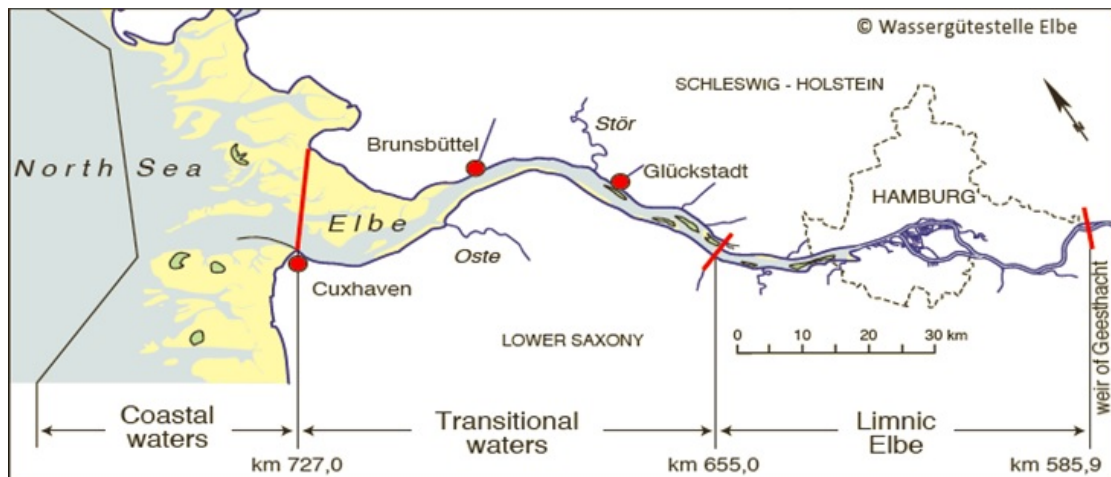
FIGURE 3.1: Map of the Elbe estuary. Source: Deltares (2011)

3.1 Modelling the Elbe estuary

3.1.1 Estuary description

Figure 3.1 shows a map of the Elbe estuary. At the open boundary at Cuxhaven, a forced tidal wave enters the estuary from the North Sea. Here, at km 727, the beginning of the estuary was defined in this research. The tidal wave passes the port of Hamburg, around 100 km up-estuary, and is reflected at the weir at Geesthacht after 140 km. Therefore, the model uses an estuary length L_c of 140 km. As can be seen in figure 3.2, the bottom level is fairly constant with an average depth of 16.5m up to Hamburg. About 100 km upriver, there is a discontinuity in bed level due to dredging strategies. Upstream of Hamburg, the estuary has an average depth of 5m.

The width of the deep navigation channel of the estuary is approximated using an e-folding convergence length L_b, as explained in section 2.2.3. For the Elbe, L_b was estimated at 50 km (Deltares, 2011).

3.1.2 Tidal forcing

As input for the model, the phase and amplitude of the tidal forcing at the open boundary are required. These were determined from a harmonic analysis of the incoming tidal wave at Cuxhaven at km 727 on the map in figure 3.1. Only the M2 and

FIGURE 3.2: Measurements of thalweg depth of the Elbe estuary, showing along-estuary depth of the deep channel, compared to low water at the mouth of the estuary. Note that x-direction is reversed in the figure, with the closed boundary at 0 km.
Source: Vandenbruwaene et al. (2013)

M4 tidal constituents were included, since these are the dominant constituents present in the tidal forcing (Winterwerp et al., 2013).

The investigated variable was along-estuary tidal range, which also depends on other tidal constituents, such as the S2 tide (Open-University, 2001). A combination of only the amplitudes of M2 and M4 will therefore not accurately represent tidal range. To overcome this problem, both M2 and M4 amplitudes were multiplied by the same factor χ to match the data for tidal range at the seaward boundary near Cuxhaven.

3.1.3 Model equations

To simulate the tidal response, an analytical solution to the linearised, width-averaged shallow water equations was obtained, as described in chapter 2. To be able to determine tidal range, the model was run for M2 and M4 separately. Results were then implemented in formula C.3, and tidal range was determined by the method explained in section 2.3. The vertical eddy viscosity was determined globally for the M2-tide, using the iterative procedure described in section 2.2.5, and the drag coefficient c_v was modified to better match experimental data.

As will be described below, several bottom configurations were investigated. For one of these configurations, a segmented model was used. To be able to simulate the discontinuity in bed level as seen in figure 3.2, this model used two different segments with different depths. For each segment, the shallow water equations were solved separately. At the junction of the two segments, two extra constraints were specified: conservation of sea level and conservation of mass. With these extra constraints, a complete solution to the shallow water equations for both segments could be obtained.
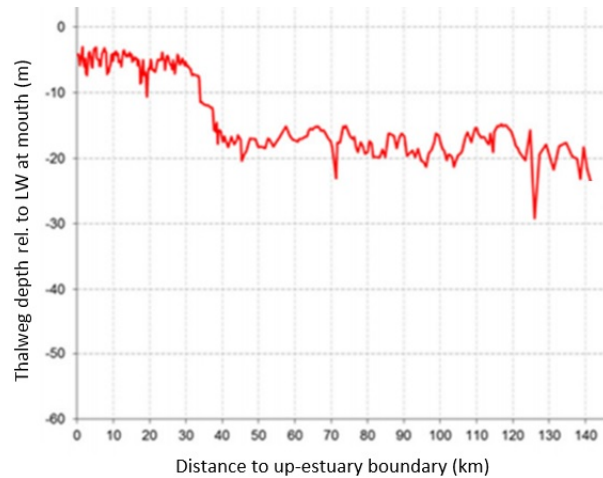
3.2 Experimental setup

3.2.1 Bottom level configurations

Tidal range was investigated for three different bottom configurations, shown in figure 3.3. The first configuration consists of a constant depth up until Hamburg, 100 km up-estuary. Here, full reflection of the tidal wave is assumed. Previous research has shown that the assumption of full reflection at Hamburg reasonably represents the observed dynamics (Deltares, 2011; Winterwerp et al., 2013). The second configuration, shown in figure 3.3b, assumes a jump in bed level at 100 km up-estuary, representing the observed discontinuity in bed level. For this scenario, the segmented model described above was applied. Part of the tidal wave is reflected against the vertical bottom wall at 100 km, but the rest of the wave travels further up-estuary and is reflected at the weir at Geesthacht. The third and last configuration, shown in figure 3.3c, consists of a constant estuary depth up to the weir at Geesthacht, at 140 km. This configuration does not represent the current situation, but might be conceived as the result of a hypothetical dredging strategy.

(A) Full reflection at Hamburg (100 km)

(B) Two depth segments

(C) Full reflection at Geesthacht (140 km)

FIGURE 3.3: Side view of the three bottom configurations that were investigated.

3.2.2 Simulations

Firstly, tidal range was computed for all three bottom configurations and compared to tidal gauge data. Next, the effect of varying depth on along-estuary tidal range in each configuration was investigated. For the first and second configuration, only estuary depth up until Hamburg was varied, in agreement with current dredging strategies as described by HPA and WSV (2012).

Lastly, the effect of a rise in global mean sea level on tidal range was investigated. As shown in figure 2.9, maximum global sea level rise in 2100 is about 1m, while a more probable scenario is a rise of about 0.5m (Church et al., 2013). Therefore, the effect of both a rise in MSL of 0.5m and 1m on tidal range were investigated for each configuration. Phase and amplitude of the changed tidal forcing (M2 & M4) were computed using the southern North Sea (ZUNO) grid in the Delft 3D model. This is a numerical model that simulates tidal dynamics on the Northwest European shelf.
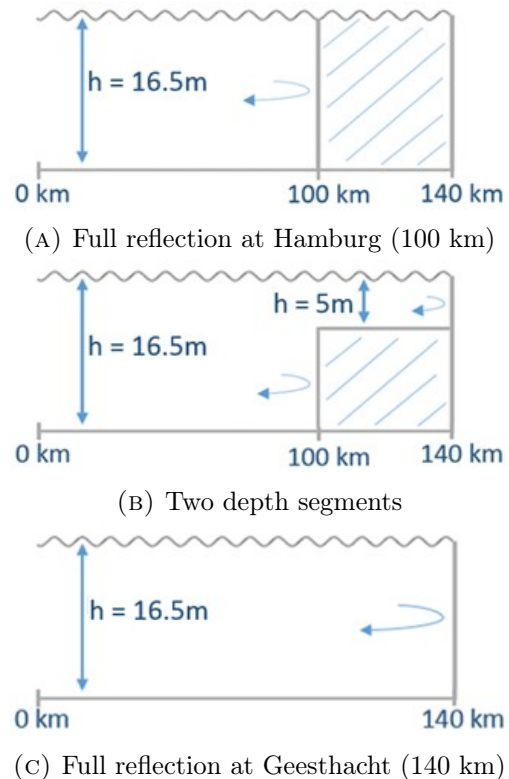
4 | Results

4.1 Tidal forcing

The phase and amplitude of the M2 and M4 tidal constituents were obtained from a harmonic analysis of the tide at Cuxhaven. Results are given in table 4.1.

Constituent	Ampl. η (m)	Phase η (deg)
M2	1.3272	11.8
M4	0.048	267.1

TABLE 4.1: Harmonic constituents at Cuxhaven that were included in the tidal forcing of the model at the open boundary

4.2 Comparison of model and data

Firstly, simulation results for tidal range for all three bottom configurations were compared to tidal gauge data, as shown in figure 4.1. The amplitudes of both M2 and M4 were multiplied by a factor $\chi = 1.12$ to represent tidal range at the open boundary, using tidal gauge data for Cuxhaven from Deltares (2011). The friction coefficient c_v was also determined by comparing simulation results to tidal gauge data, since the model uses $|u|_{x=0}$ in the linearisation of friction as described in section 2.2.5. For the first and third bottom configuration, which assume full reflection at $x = 100$ and at $x = 140$ km respectively, c_v was estimated at $3.0 \cdot 10^{-3}$. For the second configuration, that consists of two segments with different depths, c_v was estimated at $2.3 \cdot 10^{-3}$.
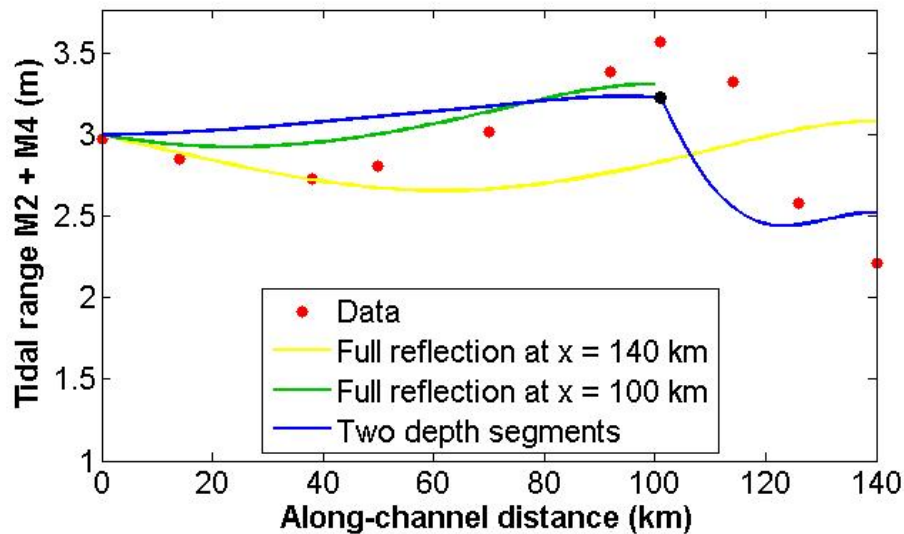

FIGURE 4.1: Simulation results for along-estuary tidal range for the three different bottom configurations. Shown in red for comparison are tidal gauge data, obtained from Boehlich (2003).

4.3   Deepening

Next, the result of deepening for each bottom configuration was investigated. Figure
4.2 shows the effect of varying depth on tidal range along the estuary, for each bottom
configuration (A)-(C). In all configurations, tidal range increases if further deepening is
carried out. For the first configuration, shown in figure 4.2a, the tide is damped for depths
lower than 13m. Maximum amplification occurs for a depth of approximately 25m; for
higher depths, amplification diminishes again. Hamburg, at 100 km, experiences the
highest tidal range for depths exceeding 13m. Results for the second configuration are
shown in figure 4.2b. In this configuration, only the depth of the first segment, up until
Hamburg, was varied. The depth of the second segment, from 100 to 140 km, was held
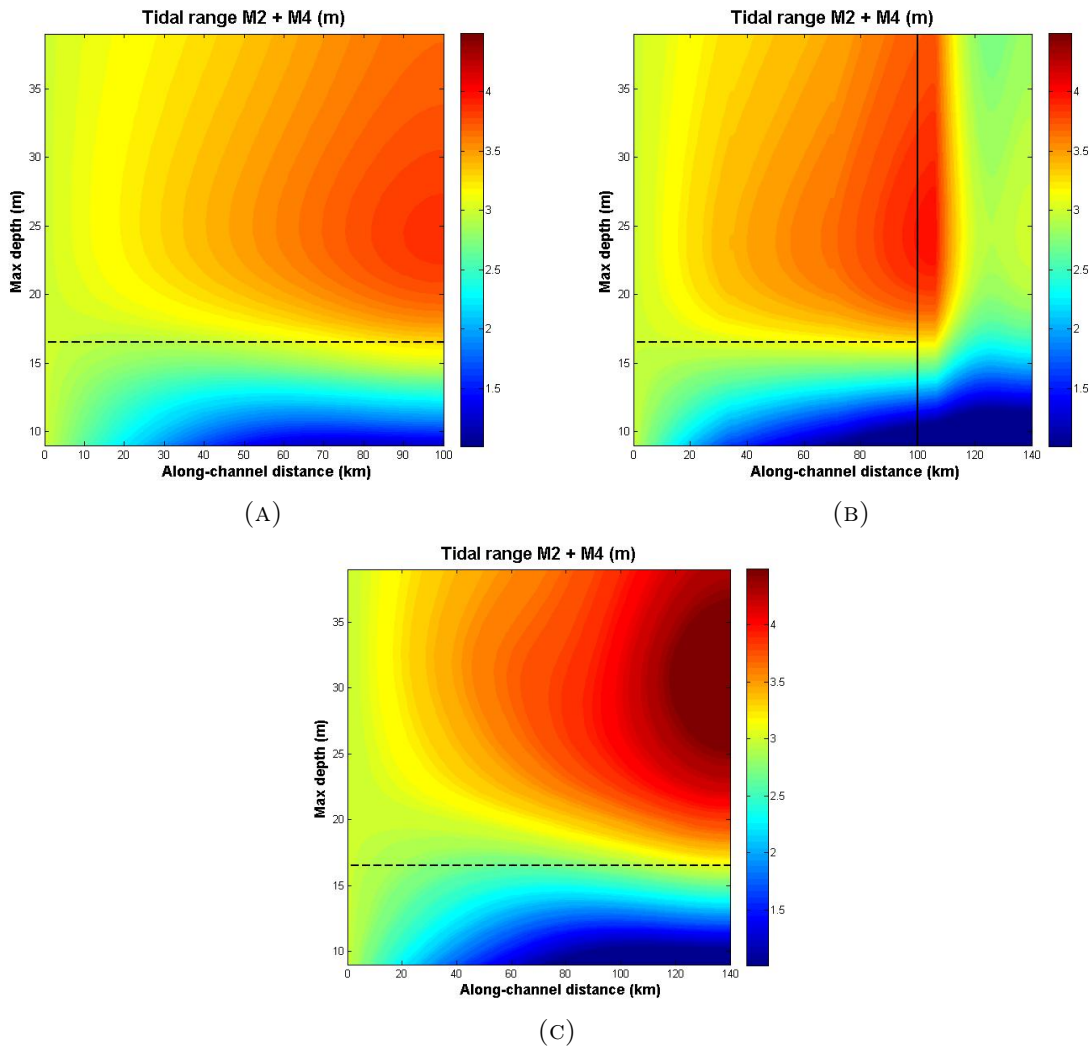

FIGURE 4.2: Contour plots showing the effect of varying depth on along-estuary tidal
range for the three investigated bottom configurations (A) - (C), as shown in figure
3.3. Color intensity indicates tidal range; the black dotted line shows the current depth
of the deep segment, 16.5m. In figure (B), the solid black line indicates the transition
between the two depth segments.

constant at 5m. Effects of deepening for the first segment in this configuration are very similar to those of the first configuration. Maximum amplification of the tide occurs in a region around Hamburg, at a depth of about 25m, and the tide is damped for depths below 13m. In the secodn segment, from Hamburg to Geesthacht (100 to 140 km), an increase in tidal range of approximately 1m occurs, if the first segment is deepened up to 25m. If the depth of the first segment exceeds 25m, tidal range for both segments decreases again. In the last configuration, shown in figure 4.2c, deepening resulted in a maximum amplification of the tide around a depth of 30m. This maximum tidal range occurs at the end of the estuary and is about 1m higher than in the first configuration. The tidal wave is attenuated for depths below 15m. A notable difference between this configuration and the former two is the tidal range at Hamburg. For depths between 15 and 20m, tidal range in the region around Hamburg is considerably lower in this configuration. However, this decrease at Hamburg is at the expense of an increase in tidal range in the region from Hamburg to Geesthacht.

4.4 Sea level rise

For each of the three configurations, the effect of a rise in mean sea level (MSL) in the North Sea of 0.5m and 1.0m on tidal range in the Elbe was investigated. Results for the changed tidal forcing for M2 and M4 as computed by the ZUNO grid in the Delft 3D model can be seen in table 4.2.

	Amplitude η_{M2} (m)	Amplitude η_{M4} (m)	Phase $\phi_{M4} - 2\phi_{M2}$
No SLR	1.3272	0.1048	234.5
SLR of 0.5m	1.4215	0.1082	345.2
SLR of 1.0m	1.4961	0.1122	358.9

TABLE 4.2: Amplitudes and phase difference for the M2 and M4 tidal constituents at Cuxhaven for a SLR of 0.5m and a SLR of 1.0m, as computed by the ZUNO grid in the Delft 3D model.

Using this tidal forcing, tidal range along the estuary was simulated for each bottom configuration for both SLR scenarios, of which results are shown in figure 4.3. The three figures show tidal range for each of the three bottom configurations. It is clear that for each case, sea level rise will lead to an increase in tidal range. Effects occurring for the 0.5m SLR scenario are similar but amplified in the 1.0m scenario.

For the bottom configurations with full reflection at $x = 100$ and $x = 140$ km, shown in figure 4.3a and 4.3c, the minimum tidal range shifts slightly up-estuary for rising sea level. Besides, tidal range increases equally along the estuary. Of all three configurations, the last one shows lowest tidal range for each SLR scenario.

In the bottom configuration with two different depth segments, shown in figure 4.3b, the tidal curve is also shifted upward for rising mean sea level. In the second segment, from $x = 100$ km to $x = 140$ km, the increase in tidal range is significantly larger than in the first segment. The minimum of the tidal curve shifts slightly seaward for rising MSL.
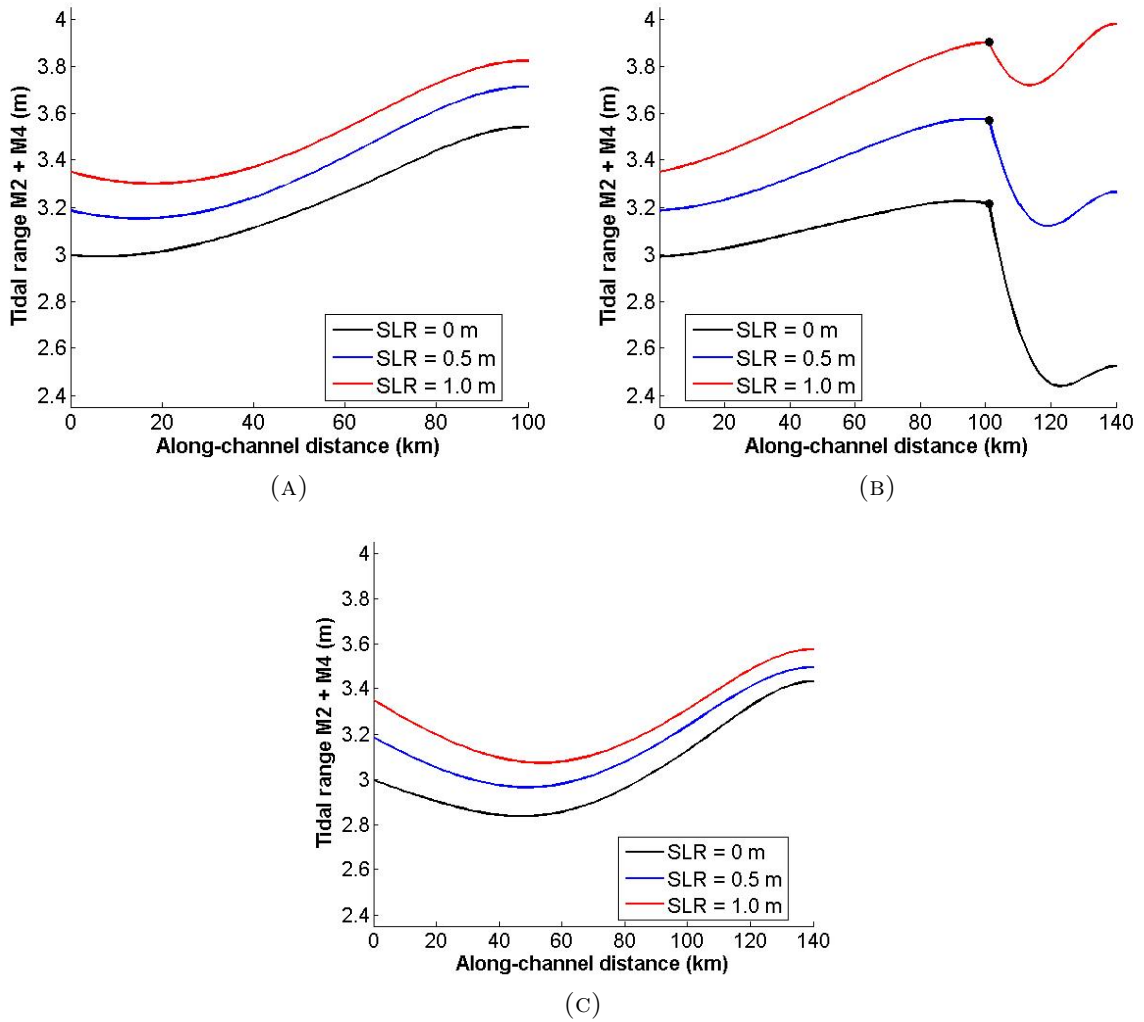

(A)

(B)

(C)

FIGURE 4.3: Effect of imposed sea level rise of 0.5m (blue) and 1.0m (red) on tidal range for the three different bottom configurations (A)-(C), as explained in figure 3.3. For comparison, the current situation (no SLR) is shown in black. Tidal forcing consisted of M2 and M4 constituents, and changes in amplitude and phase of tidal forcing due to SLR were also included.

5 | Discussion

5.1 Comparison of model and data

The tidal gauge data were reasonably represented by the simulations, as shown in figure 4.1. The tidal curve was best represented by the configuration that assumed full reflection at Hamburg. This configuration showed a slight decrease of tidal range after Cuxhaven, followed by a stronger increase up to Hamburg. However, both the modelled decrease after Cuxhaven and the computed maximum tidal range at Hamburg were lower than the tidal gauge data indicate. This is probably due to an overestimate of the effect of convergence in the outer estuary, and an underestimate of convergence in the region around Hamburg. In the model, one convergence length was chosen for the entire estuary, but data from Deltares (2011) indicate that the along-estuary convergence is not homogenous. Winterwerp et al. (2013) also suggested that the increase in tidal range around Hamburg might be due to a sharp change in convergence length. The many waterways of Hamburg's harbour, and the split-up of the Elbe here in two major branches, might have a significant effect on the tidal range.

The same mechanism can explain the differences between computed and measured values for tidal range up to Hamburg in the second configuration. Besides, this configuration reasonably represents the strong decrease in tidal range after Hamburg. The model uses a discontinuity in bed level at $x = 100$ km, where in reality, bed level increases more gradually. A gradual increase in bed level, however, could not be simulated with the assumptions in the linearised analytical model that was used.

Results for the third configuration show a strong decrease in tidal range around Hamburg, compared to current gauge data. At the same time, however, tidal range up-estuary of Hamburg increases. This configuration corresponds to a hypothetical dredging strategy, with a constant depth up to Geesthacht. Currently, dredging activities only take place up to Hamburg. Since high tidal range at Hamburg poses a problem, as stated by HPA and WSV (2012), the results show that it would be interesting to investigate with a more sophisticated model how deepening in the region up-estuary of Hamburg would influence tidal range in the rest of the estuary.

5.2 Deepening versus sea level rise

Results for the effect of depth variation on tidal range are in agreement with data from Winterwerp et al. (2013), who compared historical estuary depths and tidal gauge data. The results indicate that in each configuration, further deepening would bring the estuary

closer to resonance and thus leads to an increase in tidal range. The maximum increase is about 1m in the region around Hamburg, for a depth increase to around 25m. Since computed values for tidal range around Hamburg were low compared to gauge data, the actual increase might be bigger than the computed value. Tidal range increases most at the end of the estuary, due to the combined effect of reflection, convergence and friction.

For rising sea level, the M2 and M4 amplitudes at Cuxhaven are expected to rise due to shifts in location of the M2 amphidromic point in the North Sea (Pickering et al., 2012). This leads to an overall increase in tidal range, next to the rise in mean water level that is already induced by the SLR.

For the region around Hamburg, the 0.5m and 1.0m SLR scenarios yield the same tidal range as a deepening to 20m and 25m, respectively. Because the M2 & M4 amplitudes increase all along the estuary in the case of SLR, the increase in tidal range at the start of the estuary is stronger for SLR than for deepening. The same applies to the region beyond Hamburg. Because only the effect of deepening up to Hamburg was investigated, deepening had relatively little influence on tidal range in the region up-estuary of Hamburg. However, since the current depth in this segment is around 5m, a SLR of 0.5 to 1.0m will result in a relatively strong variation of the effective depth. This leads to a much stronger increase of tidal range in this segment when sea level rises.

The relative amplification of the tide due to SLR is not as strong as would be expected from the deepening results. For increasing SLR, the relative increase in tidal range is smaller than for increasing depth. This difference can be attributed to the value of the drag coefficient c_v. For increasing tidal range, c_v becomes larger, resulting in a relatively stronger internal friction.

5.3 Contribution of M4

Tidal range in this research was computed using M2 and M4 tidal constituents, but the M4 contribution was relatively small. Figure 5.1 shows the amplitudes for M2 and M4 separately for the first configuration. As expected, resonance characteristics are different for the M4 tide; the M4 frequency is twice as large as the M2, resulting in a different tidal wavelength. Both constituents show a maximum amplitude at the end
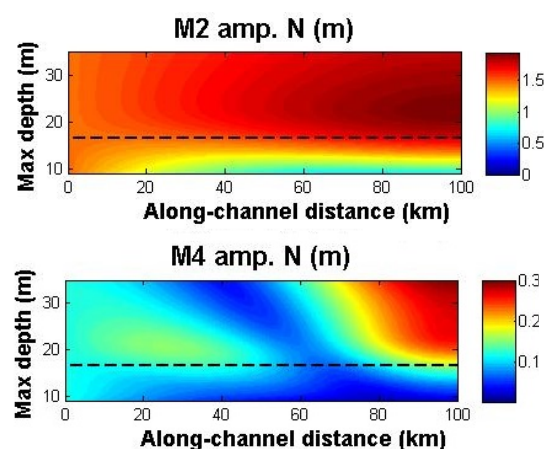

FIGURE 5.1: Effect of deepening on along-estuary amplitudes of M2 and M4 constituents, assuming full reflection at Hamburg (estuary length of 100 km). Dotted lines show current depth of 16.5m.

of the estuary, although the corresponding depths differ. For the M4 tide, a second maximum appears around 30 km up-estuary at a depth of 20m. This maximum is caused by reflection, and is less intense than the end-of-estuary maximum. This partly due to friction encountered by both the incoming and the reflected wave, and partly to convergence effects; the reflected wave experiences a broadening estuary as it travels back.

5.4 Linearisation & model approximations

This research uses a linearised analytical model, with a number of idealisations, to be able to identify the underlying physical principles of the estuary dynamics. An advanced numerical model would better match the observed dynamics, but does not give a clear insight in the underlying physics, and besides, has a much longer computation time. As stated by Schuttelaars et al. (2013), an analytical model cannot give exact predictions of tidal characteristics, but is useful to qualitatively determine the effect of proposed changes in the estuary and can indicate a number of scenarios to be investigated with advanced numerical models, such as Delft 3D.

One of the idealisations in the model is the global linearisation of vertical eddy viscosity, using the surface velocity at the open boundary of the estuary. Because this might lead to an overestimate of friction, the friction coefficient c_v was modified to better match experimental data. However, this resulted in a different friction coefficient for the different bottom configurations. Besides, local friction contributions might differ significantly due to changes in along-estuary velocity. The model could thus be improved by doing a local, instead of global, determination of the vertical eddy viscosity.

Furthermore, the model makes an estimate for tidal range by multiplying both the amplitudes of the M2 and M4 tide with a factor 1.12. In reality, tidal range is determined by the amplitude and phase of all different tidal constituents present in the tidal forcing. Although the M2 component is dominant on the Northwest-European shelf, a better estimate of tidal range could be given if more tidal constituents, such as S2, were included.

Another improvement to the model would be to account for different cross-sectional shapes. In this research, the cross-sectional shape of the estuary was rectangular, but measurements by HPA and WSV (2012) show that the shape of the navigation channel of the Elbe varies significantly along-estuary. Besides, the Elbe estuary has large intertidal flats at the seaward boundary, that flood at high water (Deltares, 2011). This results in a different estuary width during high and low water, and thus effects the water dynamics. Further research could investigate this so-called hypsometry effect in the Elbe. Besides, deepening has been shown by e.g. Burchard et al. (2004) and Kerner (2014) to influence both the free surface elevation and the velocity field. Future research could therefore also include the effect of deepening on water velocities and related implications for ecology.

6 | Conclusions

This research investigated the effect of deepening and sea level rise on tidal range in the Elbe estuary for three different longitudinal bottom profiles, using an analytical model derived from the width-averaged, linearised shallow water equations. In the tidal forcing at Cuxhaven the semidiurnal lunar tide (M2) and its first overtide (M4) were included.

Results for present-day conditions were in reasonable agreement with observed tidal range. All aspects of the tidal curve were qualitatively reproduced by the model. Differences can be attributed to local variations in estuary convergence, since the model uses one e-folding convergence length for the entire estuary. Differences could also be due to the global determination of eddy viscosity, since friction may vary locally due to along-estuary variations in velocity.

Deepening in the region up to Hamburg was found to lead to an increase in tidal range, especially in the region around Hamburg. Because the longitudinal bottom profile for the Elbe shows a discontinuity around Hamburg, the bottom configuration assuming full reflection at Hamburg could quite well represent the tidal curve. The maximum tidal range occurs at the end of the estuary, due to the combined effects of reflection and convergence.

The results also indicate that deepening in the region after Hamburg has a significant effect on the along-estuary tidal range. Since high tidal range at Hamburg currently poses a problem, as described by HPA and WSV (2012), dredging in the region from Hamburg to Geesthacht could be examined as a possible solution. However, the decrease in tidal range at Hamburg is at the expense of an increase in tidal range further up-estuary, and deepening here might have other side effects, such as changing velocity fields.

A rise in mean sea level will lead to changes in tidal characteristics in the North Sea, which is expected to induce an increase of the M2 and M4 amplitudes in the tidal forcing of the Elbe estuary (Pickering et al., 2012). This was shown to lead to an along-estuary increase in tidal range. The effects of deepening and sea level rise on tidal range were comparable for the region around Hamburg. For the region up-estuary of Hamburg, sea level rise leads to a strong increase in tidal range, due to the relatively large increase in effective depth. As Church et al. (2013) show, it is likely that mean sea level will have risen by approximately 0.5m in 2100; this has the same effect on tidal range as a deepening to around 20m, in the absence of sea level rise. The research shows that the combined long-term effects of deepening and sea level rise should be studied before new dredging activities are carried out in the Elbe estuary.

A | Linearisation of shallow water equations

Since this research focuses on the underlying physical processes of the water motion, the equations were linearised to make them analytically solvable. Linearisation is possible here because tidal amplitudes are small compared to water depth, allowing for the application of perturbation theory as explained by Friedrichs (2004). The adjustments that were made to the shallow water equations in order to linearise them, are discussed in this appendix.

The full non-linearised mass equation reads

$$\frac{\partial(b\eta)}{\partial t} = -\frac{\partial}{\partial x}b\bigg(\int_{-h}^{\eta} u \ \mathrm{d}z\bigg), \tag{A.1}$$

The right-hand side of this equation represents the along-channel volume transport, and the left-hand side represents the resulting time-rate of change in the wetted cross-sectional area, as explained in section 2.2.1. In this research the assumption was made that b does not vary with time. In most estuaries, however, the phenomenon of hypsometry occurs. This means that the wetted surface depends on sea level, and will thus vary over time. During high water, the width of the estuary is often bigger than during low water.

The second assumption is that the free surface amplitude η is small compared to water depth; $\epsilon = \frac{\eta}{h} \approx 0$. As a result, the linearised upper boundary of the integral in A.1 becomes 0 instead of η. The linearised mass equation then reads

$$b\frac{\partial \eta}{\partial t} + \frac{\partial}{\partial x}b\bigg(\int_{-h}^{0} u \ \mathrm{d}z\bigg) = 0, \tag{A.2}$$

The second governing equation is the momentum balance, which expresses the time rate of change of the velocity in terms of the relevant physical processes, and reads

$$\frac{\partial u}{\partial t} = -u\frac{\partial u}{\partial x} - g\frac{\partial \eta}{\partial x} + \frac{1}{\rho}\frac{\partial \tau_{xz}}{\partial z}, \tag{A.3}$$

where the terms on the right-hand side represent, from left to right, advection, along-channel pressure gradient and internal friction. By means of a dimensionless analysis, the advection term can be shown to be negligible when linearising equation A.3, as is also explained by Friedrichs (2004). Firstly, the advection term and the $\frac{\partial u}{\partial t}$ term are made dimensionless; the former by dividing by the typical lengthscale L_t, the tidal wavelength,

and the latter by dividing by the typical timescale T, the tidal period. The magnitude of the relative contribution of advection is then given by

$$\frac{\left[u\frac{\partial u}{\partial x}\right]}{\left[\frac{\partial u}{\partial t}\right]} \quad \sim \quad \frac{U\frac{U}{L_t}}{\frac{U}{T}} = \frac{U\ T}{L_t} \tag{A.4}$$

Using that $L_t = \sqrt{gh}\ T$, this can be rewritten as $\frac{U}{\sqrt{gh}}$, which is also known as the Froude number. According to Friedrichs (2004), in mildly nonlinear systems the Froude number is usually much less than 1 and thus the contribution of advection is negligible.

The internal friction term also gives a non-linear contribution. The shear stress τ_{xz} is a quadratic bottom stress, that scales with $|u|u$ and generates the odd harmonics. To be able to analytically solve the equations, τ_{xz} is also linearised.

[Stukje uit de theorie sectie 2.2.1 over parametrisatie van wrijving hierheen verplaatsen]

The resulting linearised momentum balance reads

$$\frac{\partial u}{\partial t} = -g\frac{\partial \eta}{\partial x} + A_v\frac{\partial^2 u}{\partial z^2}, \tag{A.5}$$

Lastly, the boundary condition for the shear stress at the free surface, introduced in section 2.2.4, states that

$$A_v\frac{\partial u}{\partial z} = 0, \qquad \text{at } z = \eta \tag{A.6}$$

Taylor expanding the derivative gives

$$\left.\frac{\partial u}{\partial z}\right|_{z=\eta} = \left.\frac{\partial u}{\partial z}\right|_{z=0} + \eta\left.\frac{\partial^2 u}{\partial z^2}\right|_{z=0} + \ ..., \tag{A.7}$$

where only the first term on the right-hand side gives a linear contribution. Therefore, the linearised boundary condition can be rewritten as

$$A_v\frac{\partial u}{\partial z} = 0, \qquad \text{at } z = 0 \tag{A.8}$$

B | Resonance lengths in non-converging estuaries

In section 2.2.2, the phenomenon of resonance in an estuary is explained. In this appendix, the condition for resonance in a frictionless non-converging estuary will be derived. The derivation will be given for the depth-averaged shallow water equations, which implies that u is now only a function of x and t, not of z.

To simplfy the equations, x = 0 is now taken at the end of the estuary, and x = L is taken at the open boundary, as shown in figure B.1.

The two governing equations are the continuity equation and momentum balance. In case of no friction, the depth-averaged momentum balance reads

$$\frac{\partial u(x,t)}{\partial t} = -g\frac{\partial \eta(x,t)}{\partial x}, \text{with } u\Big|_{x=0} = 0 \quad \text{(B.1)}$$

FIGURE B.1: Shape of estuary, indicating how x-axis is chosen.

where η represents the water level elevation, u the water velocity, g the gravitational acceleration. The boundary conditon sets the velocity at the closed boundary of the estuary to zero. The second equation is the depth-averaged continuity equation, which reads

$$\frac{\partial \eta(x,t)}{\partial t} + h\frac{\partial u(x,t)}{\partial x} = 0, \quad \text{with } \eta\Big|_{x=L} = \cos(\omega t)\hat{z}, \tag{B.2}$$

where h is the estuary depth, L the length of the estuary and ω the frequency of the forced tidal wave. The boundary condition at $x = L$ sets the water level here equal to that of the tidal forcing.

Taking the time derivative of equation B.2 and substituting $\frac{\partial u}{\partial t}$ from equation B.1, an equation for η is obtained, which reads

$$\frac{\partial^2 \eta}{\partial t^2} - hg\frac{\partial^2 \eta}{\partial x^2} = 0, \quad \text{with } \frac{\partial \eta}{\partial x}\Big|_{x=0} = 0, \tag{B.3}$$

A possible solution to equation B.3 is

$$\eta(x,t) = Z(x)\cos(\omega t), \tag{B.4}$$

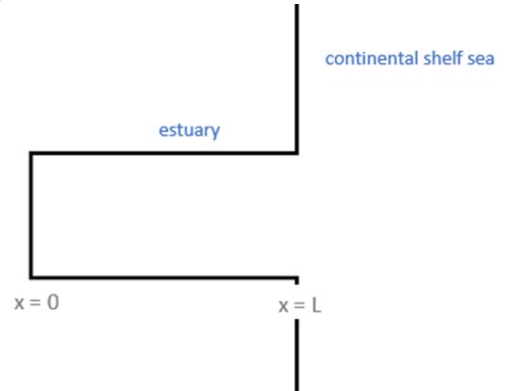where $Z(x)$ is an arbitrary function of x. Rewriting boundary conditions and implementing this solution into B.3 results in

$$\frac{\partial^2 Z}{\partial x^2} + \frac{\omega^2}{hg}Z = 0, \quad \text{with } \left.\frac{\partial Z}{\partial x}\right|_{x=0} = 0; \quad \left.Z\right|_{x=L} = \hat{z} \tag{B.5}$$

This is a second order ordinary differential equation with general solution

$$Z = A\cos(kx) + B\sin(kx), \tag{B.6}$$

where the constants A and B and the wave number k are determined by the boundary conditions; $A = \frac{\hat{z}}{\cos(kL)}, B = 0$ and $k = \frac{\omega}{\sqrt{gh}}$. The total solution for η is therefore

$$\eta(x,t) = Z(x)\cos(\omega t) = \frac{\cos(kx)\cos(\omega t)\hat{z}}{\cos(kL)} \tag{B.7}$$

The solution for u can be found by implementing B.7 into B.1 and integrating over t subsequently, and reads

$$u(x,t) = \frac{g\hat{z}\sin(kx)\sin\omega t)}{\sqrt{gh}\cos(kL)} \tag{B.8}$$

The found expressions for η and u represent the water level and velocity of the forced tidal wave; they are unbounded for $\cos(kL) = 0$ or $kL = \frac{1}{2}\pi + n\pi$. Recalling that $k = \frac{\omega}{\sqrt{gh}}$, the resulting condition for resonance is

$$\frac{\omega L}{\sqrt{gh}} = \left(n - \frac{1}{2}\right)\pi, \ n = 1, 2, ... \tag{B.9}$$

Shallow water waves travel with a speed of $\sqrt{gh}$, so the tidal wavelength L_t can be specified as

$$L_t = \sqrt{gh}\ T, \quad \text{with } T = \frac{2\pi}{\omega}, \tag{B.10}$$

where T is the period of the tidal wave. Substitution into B.8 yields the final resonance condition

$$L = \frac{1}{2}\left(n - \frac{1}{2}\right)L_t, \ n = 1, 2, ... \tag{B.11}$$

This equation shows that in a non-converging estuary, maximum resonance occurs for estuary lengths that are a quarter plus multiples of half the tidal wavelength.

C | Phase difference in tidal forcing

In this research, the M2 and M4 tidal constituents were included in the tidal forcing. This appendix will explain how the amplitudes of these constituents were combined and what the total phase difference in the tidal forcing is.

The water elevation due to the M2 tidal constituent is given by

$$\eta_{M2}(x,t) = \eta_{M2}(x)\cos(\omega_{M2}t - \phi_{M2}), \tag{C.1}$$

where η_{M2} and ϕ_{M2} are, respectively, the amplitude and phase of the M2-tide as measured at the open boundary, and ω_{M2} is the M2-frequency.

The total water elevation is the sum of the amplitudes of the different tidal constituents. Taking into account only the M2 tide and its first harmonic overtide, the equation for η_{total} reads:

$$\eta_{total}(x,t) = \eta_{M2}(x)\cos(\omega_{M2}t - \phi_{M2}) + \eta_{M4}\cos(\omega_{M4}t - \phi_{M4}) \tag{C.2}$$

By making a local coordinate transformation $\omega_{M2} \cdot t' \to \omega_{M2}t - \phi_{M2}$ and using the fact that $\omega_{M4} = 2\omega_{M2}$, this formula can be rewritten as

$$\eta_{total}(x,t') = \eta_{M2}(x)\cos(\omega_{M2}t') + \eta_{M4}\cos(2\omega_{M2}t' - (\phi_{M4} - 2\phi_{M2})) \tag{C.3}$$

Equation C.3 shows that the phase difference between the M2 and M4 tidal constituents is $\phi_{M4} - 2\phi_{M2}$.

Bibliography

Boehlich, M. J. (2003). Tidedynamik der Elbe. *Mittelungsblatt der Bundesanstalt fur Wasserbau 86*, 55–60.

Burchard, H., K. Bolding, and M. R. Villarreal (2004). Three-dimensional modelling of estuarine turbidity maxima in a tidal estuary. *Ocean Dynamics 54*, 250–265.

Church, J. A., P. U. Clark, A. Cazenave, J. M. Gregory, S. Jevrejeva, A. Levermann, M. A. Merrifield, S. A. Milne, S. R. Nerem, P. D. Nunn, A. J. Payne, W. T. Pfeffer, D. Stammer, and A. S. Unnikrishnan (2013). Sea level change. In T. F. Stocker, D. Qin, G. K. Plattner, M. Tignor, S. K. Allen, J. Boschung, A. Nauels, Y. Xia, V. Bex, and P. M. Midgley (Eds.), *Climate Change 2013: The Physical Science Basis. Contribution of Working Group I to the Fifth Assessment Report of the Intergovernmental Panel on Climate Change*. Cambridge, United KIngdom and New York, NY, USA: Cambridge University Press.

De Jonge, V. N., H. M. Schuttelaars, J. E. E. v. Beusekom, S. A. Talke, and H. E. Swart (2014). The influence of channel deepening on estuarine turbidity levels and dynamics, as exemplified by the Ems estuary. *Estuarine, Coastal and Shelf Science 139*, 46–59.

Deltares (2011). Comparison hydrodynamics and salinity of TIDE estuaries: Elbe, Humber, Scheldt and Weser. Technical report, TIDE Tidal River Development.

Friedrichs, C. T. (2004). Barotropoc tides in channelized estuaries. In A. Valle-Levinson (Ed.), *Contemporary issues in estuarine physics*. Cambridge: Cambridge University Press.

Garrison, T. (2007). *Oceanography: An Invitation to Marine Science*. Thomson Brooks/Cole.

HPA and MOW (2013, June). Joint study on mitigation measures in the estuary mouth of the Scheldt & the Elbe. Technical report, TIDE Tidal River Development.

HPA and WSV (2012, October). Dredging and disposal strategies river Elbe. Technical report, TIDE Tidal River Development.

Kappenberg, J. and H. U. Fanger (2007). *Sedimenttransportgeschehen in der tidebeeinflussten Elbe, der Deutschen Bucht und in der Nordsee*. GKSS-Forschungszentrum.

Kerner, M. (2014). Effects of deepening the Elbe estuary on sediment regime and water quality. *Estuarine, Coastal and Shelf Science 75*, 492–500.

Kreyszig, E. (2006). *Advanced engineering mathematics.* Oxford: John Wiley & Sons.

Marshall, J. and R. A. Plumb (2008). *Atmosphere, ocean & climate dynamics.* Elsevier.

Mudersbach, C., T. Wahl, I. D. Haigh, and J. Jensen (2013). Trends in high sea levels of German North Sea gauges compared to regional mean sea level changes. *Continental Shelf Research 65*, 111–120.

Open-University (2001). *Waves, tides & shallow water processes.* Oxford: Pergamon Press.

Pickering, M. D., N. C. Wells, K. J. Horsburgh, and J. A. M. Green (2012). The impact of future sea-level rise on the European shelf tides. *Continental Shelf Research 35*, 1–15.

Schuttelaars, H. M., V. N. d. Jonge, and A. Chernetsky (2013). Improving the predictive power when modelling physical effects of human interventions in estuarine systems. *Ocean & Coastal management 79*, 70–82.

Vandenbruwaene, W., Y. Plancke, T. Verwaest, and F. Mostaert (2013). Interestuarine comparison: hydrogeomorphology: Hydro- and geomorphodynamics of the TIDE estuaries Scheldt, Elbe, Weser and Humber. Technical report, Flanders Hydraulics Research: Antwerp, Belgium.

Winterwerp, J. C. and Z. B. Wang (2013). Man-induced regime shifts in small estuaries - part 1: theory. *Ocean Dynamics 63*, 1279–1292.

Winterwerp, J. C., Z. B. Wang, A. v. Braeckel, G. v. Holland, and F. Kösters (2013). Man-induced regime shifts in small estuaries - part 2: a comparison of rivers. *Ocean Dynamics 63*, 1293–1306.